Journal of Materials Processing Tech. 301 (2022) 117434

Contents lists available at ScienceDirect

Journal of Materials Processing Tech.

journal homepage: www.elsevier.com/locate/jmatprotec

Modeling of the as-cast structure and macrosegregation in the continuous casting of a steel billet: Effect of M-EMS

Zhao Zhang [a], Menghuai Wu [a,*], Haijie Zhang [a], Susanne Hahn [b], Franz Wimmer [b], Andreas Ludwig [a], Abdellah Kharicha [a]

[a] Chair of Simulation and Modelling of Metallurgical Processes, Department of Metallurgy, University of Leoben, A-8700 Leoben, Austria
[b] Primetals Technologies Austria GmbH, Turmstrasse 44, A-4031 Linz, Austria

ARTICLE INFO

Associate Editor: Prof. Alan A. Luo

Keywords:
M-EMS
Continuous casting
Billet
Solidification
As-cast structure
Macrosegregation

ABSTRACT

Mold electromagnetic stirring (M-EMS) has been introduced into the continuous casting of steel billets to promote the formation of a central equiaxed zone; however, the formation mechanism of the equiaxed crystals and the effect of M-EMS on crystal transport are not fully understood. Currently, a three-phase volume average model was used to study the solidification in a billet continuous casting (195 mm × 195 mm). The modeling results showed that the main function of M-EMS in this type of billet casting is to promote superheat dissipation in the mold region, leaving the liquid core out of the mold region undercooled. Although both, heterogeneous nucleation and crystal fragmentation, are considered to be the origins of equiaxed crystals, M-EMS appeared to impact crystal fragmentation more effectively. A small portion of equiaxed crystals could be brought by the M-EMS induced swirling flow into the superheated zone (upper mold region) and remelted; most equiaxed crystals settled in the lower undercooled zone, where they continued to grow and form a central equiaxed zone. These simultaneous phenomena represent an important species/energy transport mechanism, influencing the as-cast structure and macrosegregation. Negative segregation occurred in the central equiaxed zone, positive segregation occurred at the border of the columnar zone, and a trail of negative segregation occurred in the subsurface region of the billet. Finally, parameter studies were performed, and it was found that the shielding effect of the copper mold, electrical isolation at the strand-mold interface, and relatively high electrical conductivity of the strand shell affect the M-EMS efficiency.

1. Introduction

The solidification of continuous casting is governed by extremely complex and co-related phenomena, including melt flow, heat transfer, species transport, formation of the initial strand shell in the mold region, formation of equiaxed crystals by nucleation and/or crystal fragmentation, and transport of the equiaxed crystals. According to Du et al. (2021), the solidification in the continuous casting also affects the strand-mold interfacial condition (friction state), which in turn influences the heat transfer and the build-up of stress and strain in the casting. A comprehensive review on the modeling and simulation of continuous casting was made by Thomas (2018). Mold electromagnetic stirring (M-EMS) has been introduced into continuous casting to optimize fluid flow and heat transfer, to obtain the desired strand quality. As early as 1980s, Ayata et al. (1984) performed series of field experiments to investigate the effect of electromagnetic stirring (EMS) on the macrosegregation in continuously cast bloom and billet. A wider central equiaxed crystal zone with less negative segregation was obtained with the implementation of M-EMS. Kunstreich (2003a) presented a historical review of EMS in billet, bloom and slab casters as well as some physical mechanisms of electromagnetism and fluid flow. Meanwhile, the metallurgical principles (the stirring intensity, white band and center segregation) and a review of the industrial applications and results were presented by Kunstreich (2003b). However, theoretical interpretations to the early industry practice (plant trials and field experiments), regarding the functionalities of M-EMS in billet/bloom castings, sometimes led to confusion, because some casting results from the industry practice seemed contradictory. For example, Wang et al. (2014), based on a billet casting (185 mm × 185 mm) found that M-EMS alone could sufficiently increase the central equiaxed zone from 10 to 15 % in the non-stirring case to over 45 % with the M-EMS. Wu et al. (2011), based on a billet casting (160 mm × 200 mm) with M-EMS

* Corresponding author.
E-mail address: menghuai.wu@unileoben.ac.at (M. Wu).

https://doi.org/10.1016/j.jmatprotec.2021.117434
Received 7 September 2021; Received in revised form 3 November 2021; Accepted 16 November 2021
Available online 19 November 2021

alone, found that primary and secondary dendrite arm spacings decreased greatly as increasing the electromagnetic torque, which was beneficial to the columnar -to-equiaxed transition (CET). The center segregation and porosity of billets were reduced correspondingly. However, Ayata et al. (1984), based on another billet (125 mm × 125 mm), found that M-EMS alone could only work for middle carbon steel, and for the low and high carbon steels the M-EMS has to be combined with final electromagnetic stirring (F-EMS) to achieve the desired solidification result in the central equiaxed zone. Li et al. (2006), based on a bloom casting (380 mm × 280 mm) of high carbon steel, confirmed that M-EMS worked only in combination with F-EMS. There were even rare cases where M-EMS was not recommended. Wang et al. (2021), based on a bloom casting (510 mm × 390 mm) of 20CrMnTi steel, found that F-EMS alone (without M-EMS) was sufficient to achieve optimal casting result. Interestingly, a study of An et al. (2019), based on a bloom casting (220 mm × 260 mm), shown that in addition to the combination of M-EMS and F-EMS, a so-called mechanical soft reduction (MSR) had to be implemented to get desired quality in the central region of the bloom. Li et al. (2020) also suggested a hot-core heavy reduction rolling (HHR^2) technology could be implemented during the continuous casting process. They found that both the microstructure homogeneity and uniformity of mechanical properties along the thickness of the plate were obviously improved by using the HHR^2 process. Du et al. (2008), based on a bloom casting (220 mm × 260 mm), found that the central segregation of blooms with the special combined electromagnetic stirring mode (i.e., M-EMS and F-EMS with alternating rotation direction) could be significantly reduced. A primary reason for the above contradictory results regarding M-EMS is as follows. For the commercial interest, some sensitive details about the casting process were protected from publications such as the casting format (dimensions and section geometry), M-EMS operation parameters, alloy details, and even casting parameters (temperature and speed). This missing information is critical for understanding this process. The main reason for the above contradictory results is that the formation mechanism of the equiaxed crystals and the effect of M-EMS on crystal transport are not fully understood.

It is not possible to observe the solidification process during continuous casting with field experiments owing to the harsh environment and high cost. Therefore, numerical modeling has become an effective tool for this purpose. The first numerical model, which combines the solutions of the Maxwell, Navier-Stokes, and k–ε turbulence equations, was introduced by Spitzer et al. (1986). This early model provides valuable information for the initial stirrer design. Follow-up numerical studies focused on parameter optimization of the M-EMS process. An et al. (2018) used a three-dimensional mathematic model to investigate the effect of the applied electrical current density and frequency on melt flow. The inner quality of as-cast billet (180 mm × 180 mm) was significantly improved under the optimal parameter of 320 A and 3 Hz. Wang et al. (2020a) developed a coupled model to study the effect of stirrer position on electromagnetic field distribution, fluid flow, temperature distribution, inclusion removal and mold-level fluctuation in billet (180 mm × 220 mm) continuous casting. They found that the lower stirrer position could promote the superheat dissipation, reduce the probability of slag entrapment, and increase the removal ratio of inclusions. Trindade et al. (2002) investigated the shielding effect of copper mold based on a finite-element model, and found the increase of operating copper temperature gave rise to a magnetic field increase. Unfortunately, the above studies ignored solidification, which should be included in the solution.

The importance of considering solidification in numerical models for continuous casting has been addressed recently. Janik and Dyja (2004) used an enthalpy-based mixture model to analyze the temperature field and the growth of solid shell. They found that a three-dimensional numerical analysis is necessary because the heat flux density is not equal to zero in the casting direction. A coupled magnetohydrodynamic (MHD) model was used by Li et al. (2018) to study the characteristics of the electromagnetic field, turbulent flow, and solidification in the mold, and it was demonstrated that the area of flow field influenced by M-EMS decreased remarkably when solidification was considered. Trindade et al. (2017) used a numerical model based on finite volume element method to investigate the fluid flow and temperature distribution. They found that M-EMS decreased the temperature in the strand center and locally reduced the shell thickness due to the increase of tangential velocity close to the walls. Zhang et al. (2019) used a multi-physical mathematical model to investigate the macro transport phenomena in a billet continuous casting. They found that the high-temperature zone shifted upward with increasing M-EMS current density, and the subsurface negative segregation due to the intensive wash effects of the flow on the initially solidified shell became more severe. Fang et al. (2017) used a multiphysics numerical model to study the effect of M-EMS on flow, temperature field, solidification behavior and solute concentration field in bloom casting (380 mm × 280 mm). They found that the distribution of temperature, solute, and solidified shell was more uniform in the M-EMS effective region. However, they did not find the improvement of the centerline segregation by the M-EMS in this bloom casting. Zappulla et al. (2020) used a multiphysics model to determine the realistic temperature and stress distributions in the solidifying shell of stainless steel. They found that the stresses arising during solidification of the stainless steel include a second subsurface compression peak through the shell thickness. A common drawback of previous models is that the multiphase nature of solidification was simplified. Only the formation of the strand shell was considered, while the formation of equiaxed crystals and their transport by the M-EMS-induced flow were ignored.

The importance of the proper implementation of M-EMS in solidification models was also numerically studied. For example, the copper mold has a lower electrical conductivity at the operating temperature (~ 150 °C) than at room temperature. This implies that the shielding effect of the copper mold on M-EMS could be overestimated by considering the electrical conductivity of the mold at room temperature. Sun and Zhang (2014) used a coupled mathematical model to study the macrosegregation and macroscale transport phenomena in the bloom continuous casting of high-carbon GCr 15 bearing steel. They found that the mold temperature should be set as 423 K to meet the real continuous casting condition. Thomas et al. (2015) performed several laboratory experiments, in combined with large eddy simulations (LESs) to investigate the effect of ruler electromagnetic braking (EMBr) on transient flow phenomena. They found that the flow stability problems with realistic conducting walls were lessened greatly compared to insulated walls. Wang et al. (2020b) observed that if the strand mold gap were ignored (i.e., ideal conductivity was assumed for the strand mold interface) in the bloom continuous casting with M-EMS, an unrealistic distribution (double peaks) of the electromagnetic force would be predicted along the casting direction.

In this study, a three-phase volume average model was used to study the mixed columnar-equiaxed solidification during the continuous casting of a billet. This study focused on the effect of M-EMS on the melt flow, heat and mass transfer, formation of the strand shell, and formation and transport of equiaxed crystals. The ultimate goal is to develop and validate a numerical tool that can predict the as-cast structure and macrosegregation in continuously cast steel billets.

2. Mathematical model

The industry process of continuous casting referred to a continuous production procedure for steel by solidification, but the formation of the as-cast structure and macrosegregation is by no means a steady state process, especially when complex melt flow under the effect of M-EMS is involved. Some early modeling approaches were based on the calculation of steady state thermal field to project the as-cast structural information in the strand, e.g., Peel and Pengelly (1968) predicted the solidification and temperature profile in the continuous casting of aluminium by solving the steady conduction equation, Laitinen and

Neittaanmäki (1988) used a steady-state nonlinear parabolic-type model to simulate the multiphase heat transfer during solidification in continuous cating of steel. A thin horizontal slice model based on the steady state thermal field was also recently used to study the mold transient heat transfer behavior, which was reported by Wang et al. (2012). However, when the dynamics of flow and solidification are of primary interest, the continuous casting process must be considered transiently. Thomas (2018) made a review of the state of the art in modeling these phenomena. And further emphasized the transient character in nature of the continuous casting process.

Schematic of continuous casting under the effect of M-EMS is shown in Fig.1: (a) the start stage of casting with the zoom-in view of the mixed columnar-equiaxed solidficiation, (b) the quasi-steady stage of casting. Considering the transient nature of multiphase flow and structure formation, the solidification process must be modelled transiently, and the numerical calculation must be performed from the start stage until the quasi-steady state of the casting, i.e. when the casting is withdrawn till sufficient length (> 10.75 m for the current casting format). When the process approaches quasi-steady state, the modeling results of the casting domain are analyzed with highlight.

2.1. Solidification model

A three-phase volume average model (Fig. 1 (a)), which was developed by Wu and Ludwig (2006), was used in this study. The governing equations of the solidification model, are summarized in Table 1, but descriptions of the source terms and exchange terms are presented by Wu and Ludwig (2006) in detail elsewhere. Main features/assumptions are as follows.

(1) The three phases are the steel melt (f_ℓ), the columnar phase (f_c) from which the strand shell is built, and the equiaxed crystal grains, which are treated as an additional disperse continuum phase (f_e). Their volume fractions sum up to one.

(2) The columnar phase is assumed to develop directly from the strand surface. The position of the columnar tip front is traced dynamically according to the Lipton-Glicksman-Kurz model reported by Lipton et al. (1984). The columnar phase moves at a predefined casting velocity.

(3) The equiaxed grains originate from two mechanisms: heterogeneous nucleation and crystal fragmentation. The former occurs by activating the existing nucleation seeds (inoculants) with the necessary undercooling, and the latter described by Zheng et al. (2018) is based on the flow-enhanced remelting of dendrites near the columnar tip front.

(4) A simplified envelope scheme described by Wu et al. (2019) is used to treat the dendrite morphology of the equiaxed grains. The volume ratio of the solid dendrite to the equiaxed grain envelope (f_{si}) is set to 0.3. Remelting of equiaxed grains is considered. According to Zhang et al. (2021), only the diffusion-controlled dissolution is considered in the current study, the thermally-controlled melting process described by Han and Hellawell (1997) is ignored due to the relatively lower superheat in the current casting process.

(5) The CET occurs when the volume fraction of the equiaxed grain envelope reaches the criterion ($f_e^{env} = f_e/f_{si} = 0.49$) at the columnar tip front.

(6) Solidification shrinkage is ignored, and the thermosolutal convection is modelled using the Boussinesq approach.

(7) Volume-averaged concentrations of the melt (c_ℓ), equiaxed grains (c_e), and columnar dendrites (c_c) are calculated. The macrosegregation is characterized by the segregation index $c_{mix}^{index} = (c_{mix} - c_0) \times 100/c_0$, where c_0 is the initial concentration and c_{mix} is the mixture concentration, $c_{mix} = (f_\ell \rho_\ell c_\ell + f_e \rho_e c_e + f_c \rho_c c_c)/(f_\ell \rho_\ell + f_e \rho_e + f_c \rho_c)$.

(8) The M-EMS-induced Lorentz force is calculated based on the Maxwell equations and added to the momentum equations of both, liquid melt and equiaxed phase. Due to the electromagnetic field period being much shorter than the momentum response time of the liquid/equiaxed phases, the Lorentz force (Eq. (26)) is time-averaged, which was described in detail by Li et al. (2019). In addition, to consider the effect of fluid flow on the electromagnetic field, the Lorentz force is modified by considering a factor that is related to the relative velocity between the rotational magnetic field and the tangential velocity of the melt/equiaxed phase, Eq. (7) in Table 1.

2.2. Model implementation of billet casting

A schematic of billet continuous casting with M-EMS is shown in Fig. 2. The steel composition was Fe-C-Cr-Mn, but was simplified as a binary alloy with a nominal carbon concentration of 0.53 wt.%. The material properties and operational parameters are listed in Table 2. The casting geometry (195 mm × 195 mm) corresponded to that of an industrial process. The calculation domain was limited to only 12 m from the meniscus, which covers the mold region and three subsequent secondary cooling zones (Z1 - Z3). A five-port submerged entry nozzle

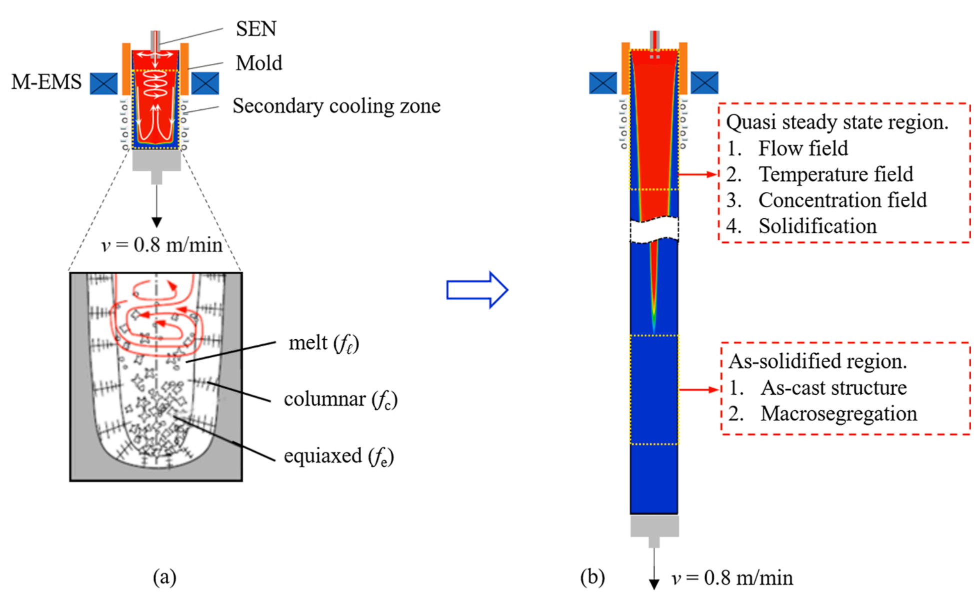

Fig. 1. Schematic of continuous casting process under the effect of M-EMS: (a) Start state of the casting with the zoom-in view of mixed columnar-equiaxed solidification; (b) Quasi-steady stage of the casting.

Table 1
Governing equations of the three-phase solidification model.

Governing equations	Symbols
1. Mass conservations: $\frac{\partial}{\partial t}(f_\ell \rho_\ell) + \nabla\cdot(f_\ell \rho_\ell \vec{u}_\ell) = -M_{\ell e} - M_{\ell c}$ (1) $\frac{\partial}{\partial t}\left(f_e \rho_e\right) + \nabla\cdot\left(f_e \rho_e \vec{u}_e\right) = M_{\ell e} + M_{ce}$ (2) $\frac{\partial}{\partial t}(f_c \rho_c) = M_{\ell c} - M_{ce}$ (3) $f_\ell + f_e + f_c = 1$ (4)	f_ℓ,f_e,f_c, volume fraction of different phase [-] ρ_ℓ,ρ_e,ρ_c, density [kg m^{-3}] $\vec{u}_\ell$,$\vec{u}_e$, velocity vector [m s^{-1}] $M_{\ell e}$,$M_{\ell c}$, net mass transfer rate (solidification) [kg m^{-3} s^{-1}] M_{ce}, net mass transfer rate (fragmentation) [kg m^{-3} s^{-1}]
2. Momentum conservations: $\frac{\partial}{\partial t}(f_\ell \rho_\ell \vec{u}_\ell) + \nabla\cdot(f_\ell \rho_\ell \vec{u}_\ell \otimes \vec{u}_\ell) = -f_\ell \nabla p + \nabla\cdot\bar{\bar{\tau}}_\ell + f_\ell \rho_\ell \vec{g}_\ell^{\,'} + f_\ell \vec{F}_L^{\,'} - \vec{U}_{\ell e} - \vec{U}_{\ell c}$ (5) $\frac{\partial}{\partial t}(f_e \rho_e \vec{u}_e) + \nabla\cdot(f_e \rho_e \vec{u}_e \otimes \vec{u}_e) = -f_e \nabla p + \nabla\cdot\bar{\bar{\tau}}_e + f_e \rho_e \vec{g} + f_e \vec{F}_L^{\,'} + \vec{U}_{\ell e} + \vec{U}_{ce}$ (6) $\vec{F}_L^{\,'} = \vec{F}_L(1 - \frac{\vec{u}_\theta}{2\pi f\cdot r})$ (7)	$\bar{\bar{\tau}}_\ell$,$\bar{\bar{\tau}}_e$, stress-strain tensors [kg m^{-1} s^{-1}] p, pressure [N m^{-2}] $\vec{g}$, gravity [m s^{-2}];$\vec{g}_\ell^{\,'}$, deduced gravity [m s^{-2}] $\vec{F}_L$,$\vec{F}_L^{\,'}$, Lorentz force and modified Lorentz force [N m^{-3}] $\vec{U}_{\ell e}$,$\vec{U}_{\ell c}$,$\vec{U}_{ce}$, momentum exchange rate [kg m^{-2} s^{-2}] $\vec{u}_\theta$, tangential velocity [m s^{-1}] f, frequency of the applied current [Hz] r, radial coordinate [m]
3. Species conservations: $\frac{\partial}{\partial t}(f_\ell \rho_\ell c_\ell) + \nabla\cdot\left(f_\ell \rho_\ell \vec{u}_\ell c_\ell\right) = \nabla\cdot(f_\ell \rho_\ell D_\ell \nabla c_\ell) - C_{\ell e} - C_{\ell c}$ (8) $\frac{\partial}{\partial t}\left(f_e \rho_e c_e\right) + \nabla\cdot\left(f_e \rho_e \vec{u}_e c_e\right) = \nabla\cdot\left(f_e \rho_e D_e \nabla c_e\right) + C_{\ell e} + C_{ce}$ (9) $\frac{\partial}{\partial t}\left(f_c \rho_c c_c\right) = \nabla\cdot\left(f_c \rho_c D_c \nabla c_c\right) + C_{\ell c} - C_{ce}$ (10)	c_ℓ,c_e,c_c, species concentration [-] D_ℓ,D_e,D_c, diffusion coefficient [m^2 s^{-1}] $C_{\ell e}$,$C_{\ell c}$,C_{ce}, species exchange rate [kg m^{-3} s^{-1}]
4. Enthalpy conservations: $\frac{\partial}{\partial t}(f_\ell \rho_\ell h_\ell) + \nabla\cdot\left(f_\ell \rho_\ell \vec{u}_\ell h_\ell\right) = \nabla\cdot(f_\ell k_\ell \nabla\cdot T_\ell) - Q_{\ell e} - Q_{\ell c}$ (11) $\frac{\partial}{\partial t}\left(f_e \rho_e h_e\right) + \nabla\cdot\left(f_e \rho_e \vec{u}_e h_e\right) = \nabla\cdot\left(f_c k_e \nabla\cdot T_e\right) + Q_{\ell e} + Q_{ce}$ (12) $\frac{\partial}{\partial t}\left(f_c \rho_c h_c\right) = \nabla\cdot\left(f_c k_c \nabla\cdot T_c\right) + Q_{\ell c} - Q_{ce}$ (13)	h_ℓ,h_e,h_c, enthalpy [J kg^{-1}] k_ℓ,k_e,k_c, thermal conductivity [W m^{-1} K^{-1}] $Q_{\ell e}$,$Q_{\ell c}$,Q_{ce}, energy exchange rate [J m^{-3} s^{-1}]
5. Formation/transport of the equiaxed grains $\frac{\partial}{\partial t}n_{eq} + \nabla\cdot\left(\vec{u}_e n_{eq}\right) = N_{nu} + N_{frag} + N_{des}$ (14) $\frac{\partial}{\partial t}n_{in} + \nabla\cdot\left(\vec{u}_\ell n_{in}\right) = -N_{nu} - N_{des}$ (15) 5.1 Heterogeneous nucleation $N_{nu} = \frac{D(\Delta T)}{Dt}\cdot\frac{dn_{eq}}{d(\Delta T)}$ (16) $\frac{D(\Delta T)}{Dt} = \frac{\partial(\Delta T)}{\partial t} + m\cdot\vec{u}_\ell\cdot\nabla c_\ell - \vec{u}_\ell\cdot\nabla T_\ell$ (17) $\frac{dn_{eq}}{d(\Delta T)} = \frac{n_{in}}{\sqrt{2\pi}\cdot\Delta T_\sigma}\cdot e^{-\frac{1}{2}\cdot\left(\frac{\Delta T - \Delta T_N}{\Delta T_\sigma}\right)^2}$ (18) 5.2 Crystals fragmentation $N_{frag} = \frac{-\gamma\cdot\left(\vec{u}_\ell - \vec{u}_c\right)\cdot\nabla c_\ell}{\frac{\pi}{6}\left(\lambda_2\cdot f_c\right)^3}$ (19) 5.3 Remelting/grain-destruction $N_{des} = v_{Re}\frac{dn_{eq}}{dx}\big\vert_{x=d_{e,critical}}$ (20) $\frac{dn_{eq}}{dx} = \frac{n_{eq}}{\sqrt{2\pi}\cdot\sigma_g\cdot x}\cdot e^{-\frac{1}{2}\cdot\left(\frac{\ln(x) - \ln(\widehat{d}_e)}{\sigma}\right)^2}$ (21) $v_{Re} = \frac{D_\ell}{R_e}\cdot\frac{(c_\ell^* - c_\ell)}{(1-k)c_\ell^*}$ (22)	n_{eq}, equiaxed number density [m^{-3}] n_{in}, inoculant number density [m^{-3}] N_{nu}, heterogeneous nucleation rate [m^{-3} s^{-1}] N_{frag}, crystals fragmentation rate [m^{-3} s^{-1}] N_{des}, equiaxed crystals destruction rate [m^{-3} s^{-1}] m, slope of liquidus in phase diagram [K (wt.%)$^{-1}$] ΔT, constitutional undercooling [K] ΔT_N, undercooling for maximum equiaxed nucleation rate [K] ΔT_σ, Gaussian distribution width of nucleation law [K] γ, fragmentation coefficient [-] λ_2, secondary dendritic arm spacing [m] v_{Re}, grain grow speed (negative value during remelting)[m s^{-1}] σ_g, geometric standard deviation of the lognormal distribution [-] x, grain diameter of different size classed [m] $\widehat{d}_e$, geometric mean of the grain size [m]
6. Electromagnetic field: $\vec{B} = \mu_0 \mu_r \vec{H}$ (23) $\nabla\times\vec{E} = -\frac{\partial\vec{B}}{\partial t}$ (24) $\vec{J} = \sigma\vec{E}$ (25) $\vec{F}_L = \frac{1}{2}R_e\left(\vec{J}\times\vec{B}^*\right)$ (26)	$\vec{B}$, magnetic flux density [T] $\vec{B}^*$, conjugate magnetic flux density [T] $\vec{H}$, magnetic field intensity [A m^{-1}] μ_0, magnetic permeability in vacuum [T m A^{-1}] μ_r, relative magnetic permeability [-] $\vec{E}$, electric field intensity [V m^{-1}] $\vec{J}$, induced current density [A m^{-2}] σ, electrical conductivity [Ω^{-1} m^{-1}] $\vec{F}_L$, time-averaged Lorentz force [N m^{-3}] R_e, the real part of a complex number [-]

(SEN) was used. *On-site* measurement of the magnetic flux density along the axis (Line 1) of the continuous casting machine with an empty mold at room temperature was performed to validate the configuration of the M-EMS stirrer. The numerically calculated electromagnetic field agreed satisfactorily with the measurements (Fig. 2(c)). A convective heat transfer thermal boundary condition was used in the mold region, and heat flux thermal boundary conditions were used in the secondary cooling zones (Z1 – Z3) and for commercial reasons, the values are omitted. No-slip flow boundary conditions were employed for the melt and equiaxed phase along the mold walls. The strand mold interface was treated electrically isolating.

2.3. Numerical procedure

The calculation is performed from the start of the casting. The casting is withdrawn downward vertically with a casting speed of 0.8 m/min, and the casting bending is ignored. In the current casting format, the metallurgical length, the as-cast structure and macrosegregation on cross-section (2 m above the casting bottom by considering the end effect of continuous casting) are unchanged after the casting has been withdrawn to a length of 10.75 m. It means the casting has reached a quasi-steady state afterwards. To ensure this point, the casting continues to be withdrawn to 12 m in length. All the modeling results of the casting domain are analyzed at this moment.

The M-EMS and flow solidification calculations were decoupled. First, the electromagnetic field was calculated using ANSYS Electronics. By solving the Maxwell equations, the magnetic flux density, electric current density, and time-averaged Lorentz force were obtained, but only the Lorentz force was exported for the subsequent flow solidification calculation, which was performed using ANSYS Fluent. The field of the Lorentz force was first interpolated into the mesh system of ANSYS Fluent, then weighted by the corresponding phase volume fraction (melt, equiaxed or columnar), and finally added as a source term to the momentum conservation equation of each phase via User-Defined Functions (UDF). To consider the effect of the motion of metal phases on the induced Lorentz force, a simple modification was made by considering a factor that is related to the relative velocity between the rotational magnetic field and the tangential velocity of the corresponding phase (Eq. (7)). For each time step (0.005 s), 20 iterations were conducted to decrease the normalized residuals of the continuity, momentum conservation, volume fraction, species transport, and user-defined scalar conservation equations to values below the convergence limit of 10^{-4} and those of the enthalpy conservation equations to below 10^{-7}. Local mesh refinements were performed near the strand wall and strand center. The minimum mesh size was set to 5 mm. The total number of finite volume elements was 529200. The eighteen "transport" quantities, f_ℓ, f_e, f_c, $u_{\ell,x}$, $u_{\ell,y}$, $u_{\ell,z}$, $u_{e,x}$, $u_{e,y}$, $u_{e,z}$, c_ℓ, c_e, c_c, T_ℓ, T_e, T_c, n_{eq}, n_{in} and pressure p, are obtained by solving the eighteen conservation equations, which are summarized in Table 1. All phases share a single pressure field, The pressure correction equation is obtained by using the "Phase Coupled SIMPLE" algorithm. To solve these multiphase coupled equations, one three-dimensional (3D) calculation (withdrawal of the casting of 12 m) required 45 days on a high-performance cluster (2.6 GHz, 28 cores).

3. Results

3.1. Flow field

The typical transient flow pattern of the steel melt inside the strand with M-EMS is shown in Fig. 3. The time-averaged Lorentz force is shown in Fig. 3(a). A symmetric Lorentz force distribution in the vertical section was obtained. The maximum force occurred near the strand surface, and decreased exponentially toward the strand center. Section views of the Lorentz force at the middle of the M-EMS system (Fig. 3 (a.2)-(a.3)) show nearly (but not perfect) axis symmetry. This deviation from perfect axis symmetry was due to the configuration of the stirrer, whose six poles were not geometrically consistent with the four corners of the strand section. Fig. 3(b) shows the complexity of the 3D flow pattern using streamlines. Four representative streamlines were analyzed in detail (Fig. 3(c)). Type A/B: The melt coming from the bottom and one side port of the SEN went directly downward. After one or two cycles of circulation in the M-EMS region, the melt continued to flow downward along the solidification front. Type C: The melt coming from one side port of the SEN impinged on the strand shell and turned upward toward the meniscus. Because it was confined by the meniscus, the melt turned back to the M-EMS region and underwent several rotations; then, it flowed spirally upward. Mainly restricted by the M-EMS, the melt could only flow back to the position near the bottom of the SEN and then flow downward to the M-EMS region. A so called "upper secondary spiral-shaped recirculation loop" was formed. This type of flow pattern was also reported by Natarajan and El-Kaddah (2004). They used a finite element analysis to investigate the electromagnetic and fluid flow phenomena in rotary electromagnetic stirring of steel. They found that the secondary flow promoted mixing beyond the region confined by the stirrer, and the extent of mixing depended on the frequency of the applied rotating magnetic field. Type D: The melt coming from one side port of the SEN flowed downward into the M-EMS region and underwent several rotations. It then flowed spirally downward along the solidification front and returned to the M-EMS region along the strand core. A so called "lower secondary spiral-shaped recirculation loop" was formed. Note that the above typical streamlines developed

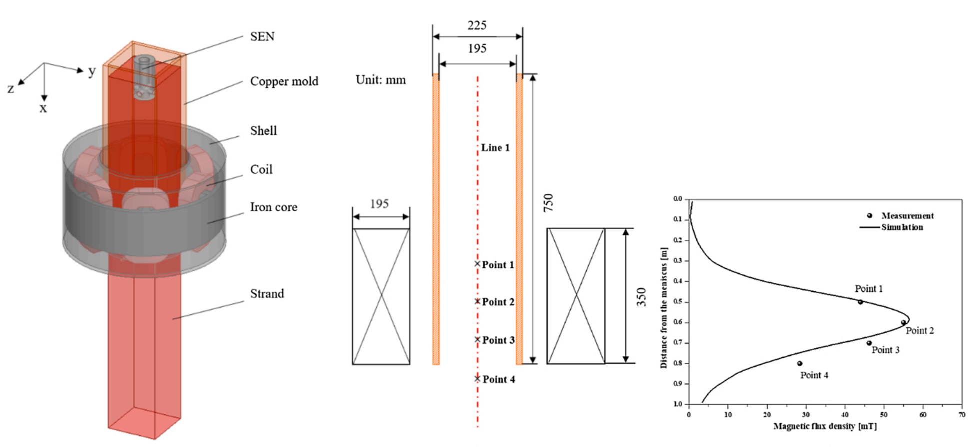

Fig. 2. (a) Schematic of billet continuous casting with M-EMS; (b) Dimensions and relative positions between the mold and M-EMS system; (c) Distribution of the measured and simulated magnetic flux densities along Line 1.

Table 2
Material properties and process parameters*.

Material properties	Symbols	Units	
Nominal concentration	c_0	wt.%	0.53
Liquidus temperature	T_L	K	1688.15
Solidus temperature	T_S	K	1593.15
Melting temperature	T_M	K	1720.15
Liquid density	ρ_ℓ	kg m^{-3}	7035.0
Density difference between melt and equiaxed crystals	$\Delta\rho$	kg m^{-3}	150.0
Latent heat	L	kJ kg^{-1}	220.0
Specific heat	c_p	J kg^{-1} K^{-1}	800.0
Thermal conductivity	k_ℓ, k_e, k_c	W m^{-1} K^{-1}	33.0
Diffusion coefficient in liquid	D_ℓ	m^2 s^{-1}	2×10^{-8}
Diffusion coefficient in solid	D_s	m^2 s^{-1}	1×10^{-9}
Thermal expansion coefficient of the melt	β_T	K^{-1}	4.5×10^{-5}
Solutal expansion coefficient of the melt	β_C	wt.%$^{-1}$	0.02
Equilibrium partition coefficient of carbon	k	–	0.252
Liquidus slope	m	K(wt.%)$^{-1}$	−60.37
Electric conductivity of strand (melt)	σ_ℓ	S m^{-1}	7.6×10^5
Electric conductivity of strand (solid)	σ_s	S m^{-1}	8.2×10^5
Electric conductivity of mold (423 K) (Li et al. (2018))	$\sigma_{m\text{-}423}$	S m^{-1}	3.18×10^7
Electric conductivity of mold (298 K) (Li et al. (2018))	$\sigma_{m\text{-}298}$	S m^{-1}	4.7×10^7
Primary dendritic arm spacing	λ_1	m	1.85×10^{-4}
Secondary dendritic arm spacing	λ_2	m	4.8×10^{-5}
Viscosity	μ_ℓ	kg m^{-1} s^{-1}	0.006
Gibbs Thomson coefficient	Γ	–	3.3×10^{-7}
Initial inoculant number density	n_{in}^0	m^{-3}	1×10^9
Initial equiaxed number density	n_{eq}^0	m^{-3}	1×10^6
Undercooling for maximum equiaxed nucleation rate	ΔT_N	K	5.0
Gaussian distribution width (nucleation)	ΔT_σ	K	3.0
Packing limit for equiaxed crystals	$f_{e,packing}$	–	0.637
Volume ratio of solid dendrite to equiaxed grain envelope	f_{si}	–	0.3
Fragmentation coefficient	γ	–	3.0×10^{-5}
Process parameters			
Strand format	D	m	0.195 × 0.195
Mold length	H_m	m	0.75
Secondary cooling zone length (Z1)	H_1	m	xxx
Secondary cooling zone length (Z2)	H_2	m	xxx
Secondary cooling zone length (Z3)	H_3	m	xxx
Casting speed	V_c	m min^{-1}	0.8
Pouring temperature	T_p	K	1708.15
AC electric current	I	A	xxx
M-EMS frequency	f	Hz	3.0

* For commercial reasons, some process parameters, including the thermal boundary conditions, are omitted.

transiently, and could change from one type to another dynamically. Further, the velocity (motion) of the equiaxed phase was not identical to that of the melt flow (Section 3.2).

For comparison, the flow pattern for the case without M-EMS is shown in Fig. 3 (d). The jet from the bottom port of the SEN flowed downward directly. Meanwhile, the melt from the side ports of the SEN impinged on the strand shell first and then split into two streams: one turned upward toward the meniscus, forming vortices below the meniscus, and the other turned downward along the solidification front. The downward flow along the solidification front drove an upward flow in the strand center.

3.2. Temperature field and solidification

The transient solidification process together with the temperature/velocity fields for the case with M-EMS are shown in Fig. 4. For comparison, the temperature field for the case without M-EMS is shown in Fig. 4(d). The analysis area was limited to 2 m from the meniscus, covering the mold region and two secondary cooling zones (Z1 and Z2).

As shown in Fig. 4(a), one important role of the M-EMS is to confine the superheated region to the mold region, leaving the liquid core below the mold undercooled. The superheated region is indicated by the enclosed liquidus isotherm (1688.15 K). Owing to the rotational electromagnetic force, the downward jet flow coming from the bottom exit of the SEN was brought back to the upper part of the mold region along the solidification front (Fig. 4(a), Zoom A). In contrast to the case with M-EMS, the superheated region in the case without M-EMS can extend through the liquid core of the strand far below the mold region (Fig. 4(d)). Similar phenomenon was also observed in direct chill casting of aluminium by Jia et al. (2020). They found that the melt temperature decreased rapidly in the presence of electromagnetic field (EMF). Thus, a shallower depth of the liquid sump was obtained.

Fig. 4(b) shows the contour of the volume fraction of the columnar phase (f_c) overlaid with the melt velocity ($\vec{u}_\ell$). An isoline ($f_\ell = 0.3$) was used to approximate the shell thickness, and another isoline ($f_\ell = 0.95$) was used to define the columnar solidification front. Therefore, the mushy zone thickness is the distance between the two isolines. Near the middle height of the M-EMS system, the swirling flow was confined by the solidified shell (Fig. 4(b), Zoom B). The high-temperature melt coming from the side ports of the SEN impinged on the strand shell and split into two opposite streams: one upward and one downward. The upward stream was confined between the strand shell, meniscus, and SEN, forming an upper vortex. The upper vortex played an important role in preventing the solidification of the meniscus. The downward stream was blocked by the upper recirculation loop generated by the M-EMS, and thus, a small lower vortex was formed (Fig. 4(b), Zoom A). In the secondary cooling zone, the lower recirculation loop generated by the M-EMS accelerated the downward flow along the solidification front, which in turn drove the melt backward into the mold region along the strand center (Fig. 4(b), Zoom C). After encountering the jet flow from the bottom exit of the SEN, the two parts of the melt joined together and were conducted toward the solidification front by the upper/lower recirculation loops (Fig. 4(b), Zoom A).

Fig. 4(c) shows the contour of the volume fraction of the equiaxed phase (f_e) overlaid with the velocity vector of the equiaxed phase ($\vec{u}_e$). A small portion of equiaxed crystals, which were generated by heterogeneous nucleation/crystal fragmentation near the columnar solidification front, was carried to the upper mold region by the upper recirculation loop (Fig. 4(c), Zoom A) and partially remelted in the superheated zone. At approximately 0.29 m below the meniscus, some equiaxed crystals could temporarily survive when they were brought into the lightly undercooled zone (Fig. 4(c), Zoom D). In the secondary cooling zone, most equiaxed crystals settled down and continued to grow during settling (Fig. 4(c), Zoom C).

The temperature profiles along the centerline and strand surface are plotted in Fig. 5, and a comparison is made between the cases with and without M-EMS. Without M-EMS, two large flow recirculation loops (Fig. 4(d), Zone A) were created on the vertical half-plane of the strand. The left recirculation loop consistently brought the cooler melt (still superheated) to the strand center. However, the cooling effect was so weak that the temperature along the centerline at the mold exit was 1706.9 K. Therefore, only 1.25 K of superheat was dissipated (Fig. 5(a)). The right recirculation loop brought hotter melt toward the solidification front, raising the surface temperature (T = 1431.15 K) at the position 0.25 m below the meniscus (Fig. 5(b)). The area of influence was only maintained for a short distance to the position 0.34 m (T = 1452.83 K) below the meniscus. Subsequently, the surface temperature dropped rapidly (Fig. 5(b)). For the case with M-EMS, two large recirculation loops were generated: one upper recirculation loop above the M-EMS system and one lower recirculation loop below the M-EMS system. The upper recirculation loop drove the cooler melt along the solidification

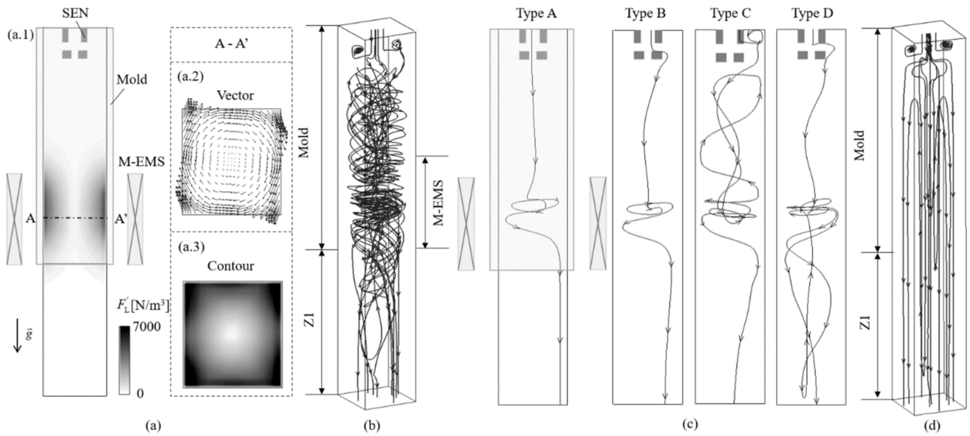

Fig. 3. Melt flow during solidification of the steel billet with M-EMS. (a) Time-averaged Lorentz force distributions on three sections; (b) Streamlines of the melt flow; (c) Four types of streamlines shown separately; (d) For comparison, the flow pattern (streamlines) without M-EMS is also shown.

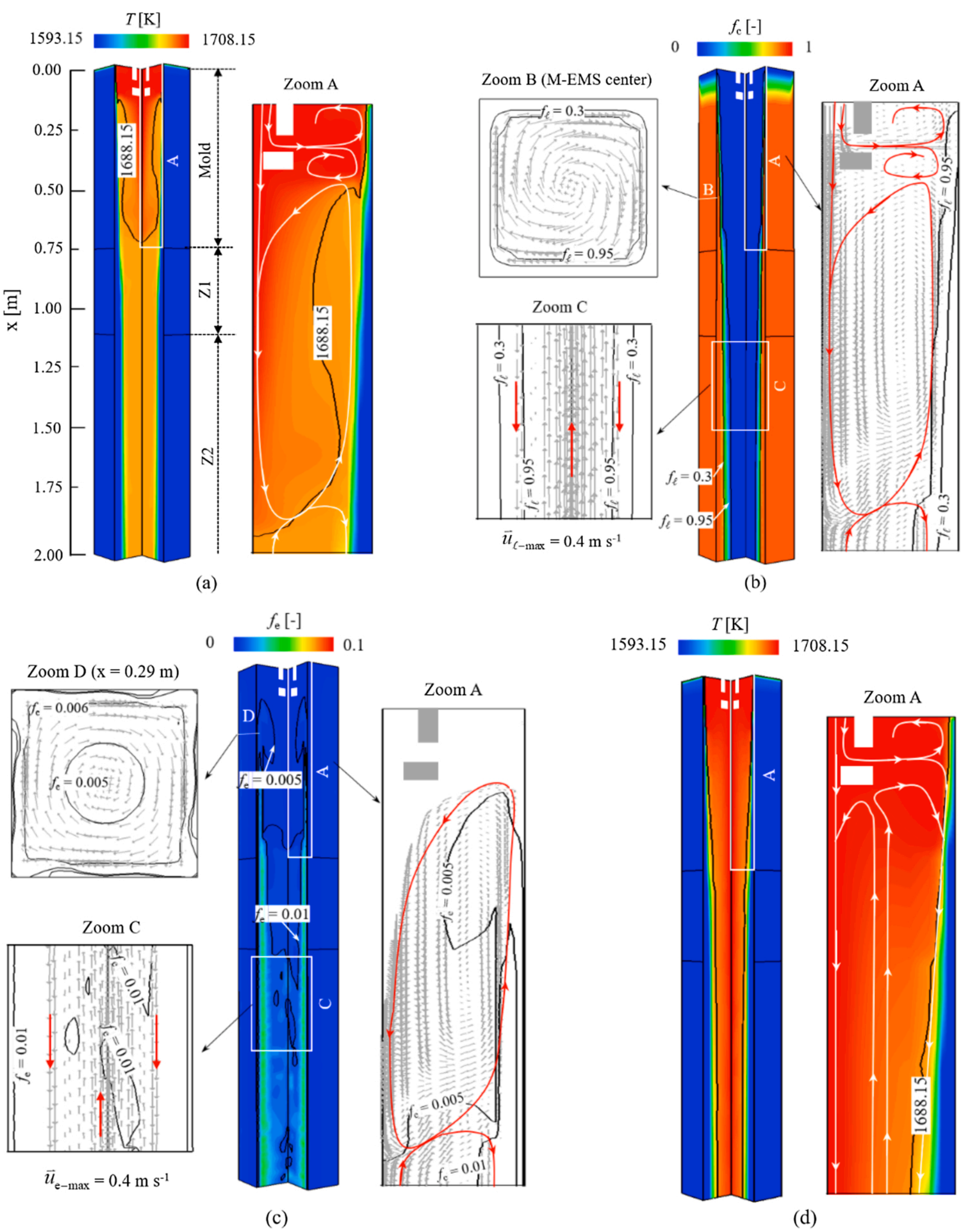

Fig. 4. Transient solidification process in the upper part of the strand with M-EMS. (a) T field overlaid with the liquidus isotherm (1688.15 K), indicating the superheated zone; (b) Volume fraction of the columnar phase (f_c) overlaid with $\vec{u}_\ell$ vectors (white) and streamlines (red) schematically highlighting the flow direction; (c) Volume fraction of the equiaxed phase (f_e) overlaid with $\vec{u}_e$ vectors (white) and streamlines (red) schematically highlighting the direction of motion of the equiaxed phase. (d) For comparison, the temperature field for the case without M-EMS is shown. (For interpretation of the references to colour in this Figure legend, the reader is referred to the web version of this article).

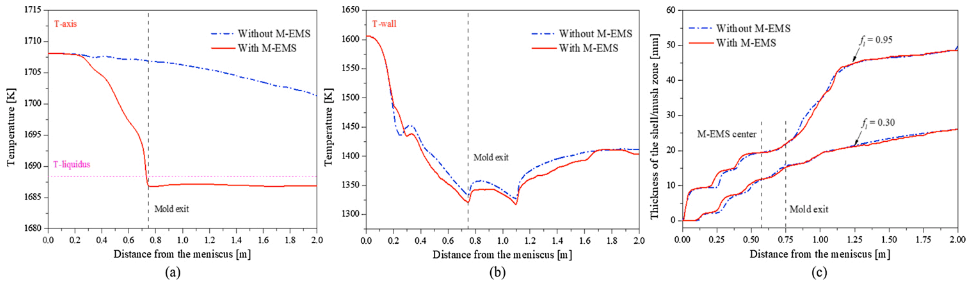

Fig. 5. Comparisons of T profiles and thicknesses of the strand shell and mushy zone between the two cases: with and without M-EMS. (a) T profiles along the strand centerline and (b) T profiles along the strand surface. (c) Thicknesses of the solid shell/mushy zone.

front to the center of the strand, which substantially decreased the temperature of the liquid core. The centerline temperature at the mold exit was 1686.79 K, which is lower than the liquidus temperature (Fig. 5(a)). This indicates that the area outside the mold region was entirely undercooled. Another role of the upper recirculation loop was to inhibit the downward flow of the melt coming from the side ports of the SEN; a small part of the melt was blocked near the SEN (Fig. 4(a)). Consequently, the temperature decreased drastically along the casting direction. One interesting finding is that for the case with M-EMS, the surface temperature of the strand in most of the mold region was slightly lower than that in the case without M-EMS. This implies that M-EMS may not increase the heat transfer rate from the strand surface to the water-cooled copper mold. In contrast, it may even slightly reduce the cooling rate from the strand surface to the mold. The surface integral of the heat flux over the entire strand surface area in the mold region was calculated, and a comparison was made between the two cases (with and without M-EMS). The results verified the above statement: M-EMS does not increase the heat transfer rate from the strand surface to the water-cooled copper mold. However, M-EMS induced flow is beneficial for the temperature homogenization in the strand. It means that the temperatures of liquid (near the solidification front) and the solid shell in the secondary cooling zone are raised under the effect of M-EMS. Part of the thermal energy (the superheat which is presented in the long hot core region for the case without applying M-EMS) is transferred to the sensible energy and stored in the solid shell and liquid phase (near the solidification front).

Fig. 5(c) shows the evolution of the solid strand shell/mushy zone thicknesses. M-EMS slightly promoted the growth of the solid shell/mushy zones above the M-EMS center, while it inhibited their growth below the M-EMS center. This phenomenon is related to the flow pattern (Fig. 3 and Fig. 4). The upper recirculation loop generated by M-EMS inhibited the downward flow of the hotter melt coming from the side ports of the SEN and drove the cooler melt upward along the solidification front. This type of flow reduces the temperature near the solidification front, which is beneficial for the growth of the strand shell/mushy zone. In contrast, the lower recirculation loop generated by M-EMS brought the hotter melt from the strand center to the solidification front and delayed the growth of the solid shell/mushy zone. The thickness of the strand shell at the mold exit was 15.26 mm with M-EMS and 16.67 mm without M-EMS. Some steps can also be observed in the curves, which were not only due to the flow effect but were also be attributed to the mesh size. In this study, a relatively refined mesh (5 mm) was used near the strand wall to calculate the growth of the solid shell/mushy zone; a relatively coarse mesh (7 mm) was used for the inner part. Note that the curves should become smoother after further mesh refinement, but the calculation cost would drastically increase, considering that the current 3D calculation required 45 days on a high-performance cluster (2.6 GHz, 28 cores).

3.3. Origin/solidification and remelting/destruction of equiaxed crystals

Fig. 6(a) shows the contour of the constitutional undercooling of the strand, $\Delta T = T_f + m{\cdot}c_\ell$ - T, where ΔT considers both, the liquid concentration and temperature. The undercooled and superheated regions are separated by the isoline $\Delta T = 0$ K. Fig. 6(b) displays the distribution of the heterogeneous nucleation rate (N_{nu}). When the necessary nucleation conditions are achieved in the undercooled region, the inoculants are activated as equiaxed crystals. Once the local inoculants are consumed, no heterogeneous nucleation will occur at this site. However, if some inoculants are brought to this site by flow from other regions, nucleation can continue again. Therefore, the distributions of N_{nu} and ΔT were very different; the former was continuous and smooth, whereas the latter was uneven and random, and mostly located in the upper part of the casting (the undercooling area). Fig. 6(c) shows the contour of the crystal fragmentation rate (N_{frag}). The fragments were located more frequently in the mushy zone near the columnar tip front along the length of the strand. Analysis of the results showed that the M-EMS-induced flow appeared to impact crystal fragmentation very effectively. To further study the role of M-EMS, N_{nu} and N_{frag} under the conditions with and without M-EMS are quantitatively compared in Table 3. Here, the volume integrals of time-averaged N_{nu} and N_{frag} (over a time interval of 7 s) in different cooling zones were performed. With M-EMS, the total creation rate of the crystal number density by the mechanism of fragmentation (N_{frag}, sum over the mold, Z1, and Z2 regions) was approximately 1.5×10^5 [s^{-1}], which is approximately one order of magnitude higher than that of the case without M-EMS. However, the total creation rate of the crystal number density by the mechanism of nucleation (N_{nu}) was similar for both cases; that is, M-EMS did not increase (or even slightly reduce) the total N_{nu}. The conclusion is that M-EMS increases the quantity of equiaxed crystals via crystal fragmentation. Regardless, most of the fragmentation events occurred in the mold region owing to the stirring effect of M-EMS. Fig. 6(d) shows the net mass transfer rate from the liquid melt to the equiaxed crystals ($M_{\ell e}$). Once equiaxed crystals form, they will continue to grow or be remelted depending on the local thermal and solutal environment. This indicates that the M-EMS-induced swirling flow provides a favorable growth environment for equiaxed crystals out of the mold region by accelerating superheat dissipation. Most of the newly formed equiaxed crystals settle into the undercooled secondary cooling zone, where they continue to grow and form the central equiaxed zone.

During the growth of equiaxed crystals, remelting/destruction of the crystals occurs when they are transported to the superheated melt region. The process involves two steps: reduction in crystal size (remelting) and destruction (disappearance) of the crystals. Fig. 7(a) displays the contour of ΔT; only the region with a negative value of ΔT (superheating) is depicted, and the region with a positive value of ΔT (undercooling) is omitted. Fig. 7(b) shows the distribution of $M_{\ell e}$. Here again, only the region with a negative value of $M_{\ell e}$ (remelting) is shown. A small portion of the newly formed equiaxed crystals was transported to the superheated region, driven by the melt flow (Fig. 4(c)). There, remelting occurred, which was accompanied by a decrease in the local temperature and a negative $M_{\ell e}$. In addition, the melting of low-concentration crystals can dilute the liquid concentration at the center of the strand. Once the crystal size is reduced to a critical value (Eq. 20),

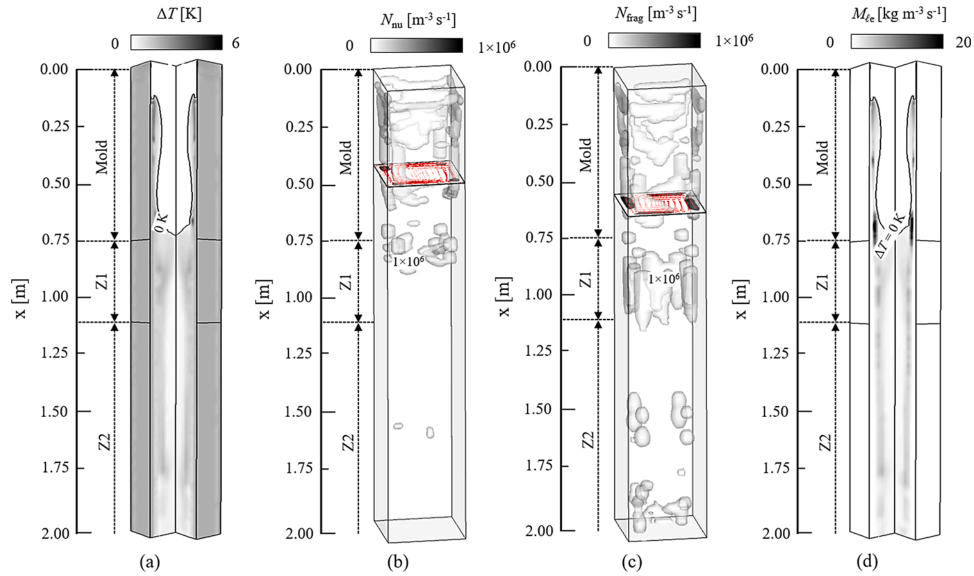

Fig. 6. (a) Contour of the constitutional undercooling ΔT; (b) Heterogeneous nucleation rate N_{nu}; (c) Crystal fragmentation rate N_{frag}; (d) Net mass transfer rate from the melt to the equiaxed crystals $M_{\ell \mathrm{e}}$ (solidification).

Table 3
Time-averaged heterogeneous nucleation rate and crystal fragmentation rate in various cooling zones.

Mechanism		Mold region	Z1	Z2	Total
Heterogeneous nucleation rate [s^{-1}]	With M-EMS	95474.63	10392.85	441.63	106309.11
	Without M-EMS	112719.39	17837.36	7797.13	138353.88
Crystal fragmentation rate[s^{-1}]	With M-EMS	99498.49	42017.89	5138.75	146655.13
	Without M-EMS	6712.56	5498.22	2026.22	14237.00

the equiaxed crystals will be destroyed and converted into inoculants (Eqs. 14–15). Fig. 7(c) depicts the distribution of the destruction rate of equiaxed crystals (N_{des}); its profile is similar to that of the remelting rate of the crystals.

3.4. As-cast structure and macrosegregation

Fig. 8(a) displays an experimental macrograph of the as-cast structure (with M-EMS). The columnar, mixed, and equiaxed regions are marked with dotted lines based on the authors' subjective judgment of the macrograph. Fig. 8(b) shows the simulated macrostructure for the case with M-EMS, and Fig. 8(c) displays the simulated macrostructure for the case without M-EMS. For the simulation cases, the equiaxed zone is marked by the isoline of the equiaxed grain envelope: $f_{\mathrm{e}}^{\mathrm{env}} = 1.0$; the columnar and mixed zones are distinguished by the isoline of the equiaxed grain envelope: $f_{\mathrm{e}}^{\mathrm{env}} = 0.17$. In this study, the equiaxed zone ratio was defined as the area ratio of the equiaxed zone to the entire cross section (195 mm × 195 mm). When M-EMS was applied, the profile of

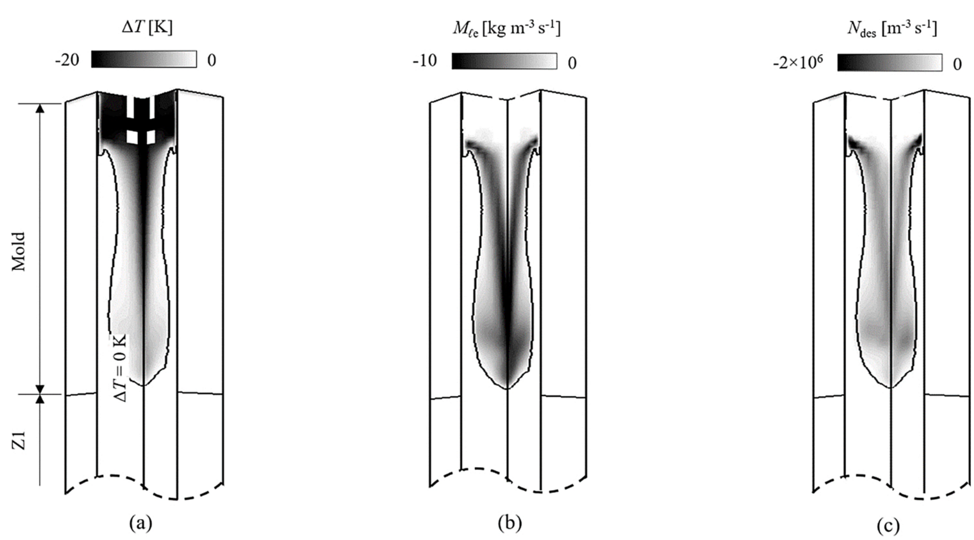

Fig. 7. (a) Contour of the undercooling degree ΔT (negative scale). (b) Net mass transfer rate from the melt to the equiaxed crystals $M_{\ell \mathrm{e}}$ (remelting). (c) Destruction rate of the equiaxed crystals N_{des}. The simulation result is shown in grey-scale, with dark for the superheated region and remelting/destruction rate. Only the simulation results in the superheated region are shown. The results in the undercooled region with nucleation and fragmentation are not shown.

the columnar zone showed a satisfactory agreement with the one of the as-cast structure. The experimentally measured area ratio of the equiaxed zone was approximately 22.03 % (Fig. 8(a)), while the simulated value was 12.6 % (Fig. 8(b)), the equiaxed zone was underestimated by the simulation. Without M-EMS, the equiaxed zone ratio was relatively low (2.3 %); that is, the entire strand section was nearly full of the columnar structure. This would lead to the generation of centerline porosity.

Fig. 9(a) depicts the contour of the macrosegregation index for the two cases: with and without M-EMS. Fig. 9(b) shows the distribution of the macrosegregation index along the symmetry line (Line 2) of the strand section. Because of the accumulation of equiaxed crystals, negative segregation occurred in the central equiaxed zone, positive segregation occurred at the border of the columnar zone, and a trail of negative segregation (white band) occurred in the subsurface region of the billet. For the case without M-EMS, the macrosegregation was weaker, and severe negative segregation only occurred in the central equiaxed zone. The averaged surface integrals of the macrosegregation index ($\sum \Delta A \cdot c_{\mathrm{mix}}^{\mathrm{index}} / \sum \Delta A$) at the strand section were performed for the two cases. The value is -0.024 % for the case with M-EMS, and -0.03129 % for the case without M-EMS.

4. Discussion

4.1. Transport phenomenon caused by solidification, migration, and remelting of equiaxed crystals

During the continuous casting of steel billets under M-EMS, the formation, growth, migration, and remelting of equiaxed crystals in the mold region represent an important mechanism of mass and energy transport, which impacts the as-cast structure and macrosegregation. As schematically shown in Fig. 10(a), the equiaxed crystals can (1) originate mainly from fragmentation (N_{frag}) in the intensive M-EMS region and partially from nucleation (N_{nu}) in the upper mold region, (2) grow in the undercooled zone along the columnar tip front, (3) migrate to the central superheated region below the SEN owing to the special flow pattern (M-EMS-induced circulation loop between the SEN and the stirrer), and (4) finally remelt in the strand center. The modeling results of N_{nu}, N_{frag}, f_{e}, $M_{\ell\mathrm{e}}$, and N_{des} are also shown in Fig. 10(a)-(b), which support the above statement. Typically, the as-formed equiaxed crystals, which are heavier than the liquid, settle downward. However, the swirling flow and recirculation loop induced by M-EMS greatly influence the motion of these crystals. A small portion of equiaxed crystals was brought to the upper part of the mold region and remelted/destroyed in the superheated region.

It is known that the solidification of equiaxed crystals releases latent heat and rejects the solute element (the solute partition coefficient $k <$ 1). In contrast, the remelting of equiaxed crystals absorbs latent heat and dilutes the solute concentration. These two events, that is, solidification and remelting, occur in different locations: one at the solidification front and one in the strand center. Therefore, the migration of equiaxed grains, which bridges the above two events, represents an important energy/species transport mechanism. To demonstrate the importance of the above mechanism, one more simulation case was considered, where remelting/destruction was not factored. Fig. 11 compares the T field, net mass transfer rate ($M_{\ell\mathrm{e}}$), and liquid concentration field (c_{ℓ}), between two simulation cases: one with and one without remelting. The undercooling zone in the upper part of the mold region, which was caused when the upper recirculation loop generated by M-EMS (Fig. 4(a)) was larger when remelting was considered (Fig. 11(a)). In other words, the superheated region was somehow "compressed" toward the strand center owing to the cooling effect (absorption of latent heat) induced by the remelting of equiaxed crystals. The nominal concentration of the melt from the SEN was 0.0053. As shown in Fig. 11(c), c_{ℓ} in the superheated region was higher when the remelting of equiaxed crystals was considered. The modeling results in Fig. 11 may not sufficiently demonstrate the differences between the two cases because the differences in T and c_{ℓ} can subsequently impact further solidification in the secondary cooling zones of the strand. In summary, the solidification, migration, and remelting of equiaxed crystals play a vital role in the redistribution of energy (temperature) and liquid concentration. It should be acknowledged that omitting these phenomena results in considerable error in the prediction of the final as-cast structure and macrosegregation.

4.2. Consideration of the state-dependent electrical conductivity of the solidified shell

Steel has a higher electrical conductivity (σ) in the solid state than that in the liquid state, and the difference in σ is approximately 7.8 % for this alloy. This implies that the electric current path induced by M-EMS may vary during the evolution of the solid shell. To understand the influence of the state-dependent σ on the efficiency of M-EMS, two simulation cases were compared. The first case assumed a uniform electrical conductivity (7.6 × 10^5 S/m), independent of the liquid/solid state. The second case used the state-dependent electrical conductivity for different regions; that is, the as-solidified shell used the value of the solid state (8.2 × 10^5 S/m). To achieve the second case, an iterative calculation between two software packages (ANSYS Electronics and ANSYS Fluent) was performed. The profile of the solid shell calculated from the first case was taken as a reference to update the distribution of the Lorentz force with ANSYS Electronics, considering the state-dependent σ. The updated Lorentz force was used to calculate the solidification of the strand. Fig. 12 shows the time-averaged magnitude of the magnetic flux density (B), induced electrical current density (J), and

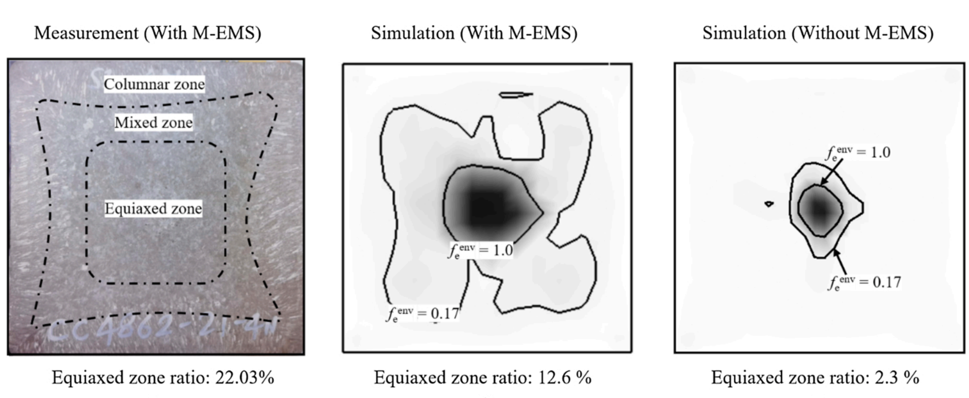

Fig. 8. (a) Macrograph of the as-cast structure with M-EMS. (b) Simulated macrostructure for the case with M-EMS. (c) Simulated macrostructure for the case without M-EMS.

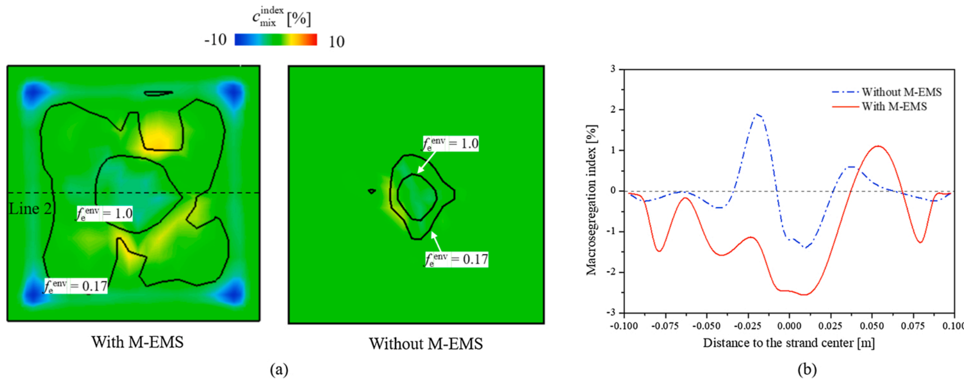

Fig. 9. (a) Contour of the macrosegregation index for the two cases: with and without M-EMS; (b) Distribution of the macrosegregation index along the centerline (Line 2) of the strand section.

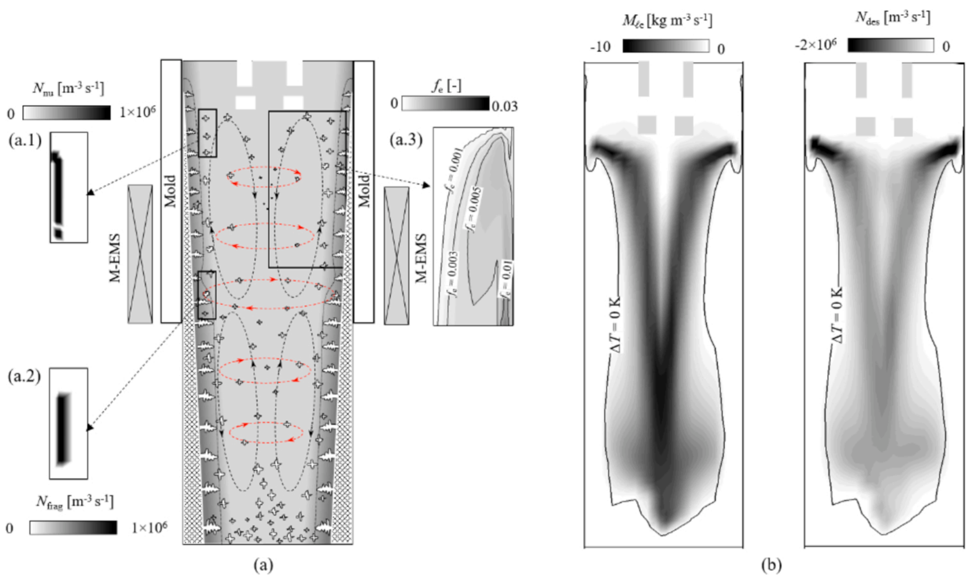

Fig. 10. (a) Schematic of the mass/energy transport mechanism through the formation/growth, migration, and remelting of equiaxed crystals under the effect of M-EMS. The red/black dashed lines highlight the motion/migration direction of equiaxed crystals, and the black dotted line defines the columnar tip front. (b) Calculated remelting rate ($M_{\ell e}$) and grain destruction rate (N_{des}) of equiaxed crystals in the superheated region. Only the range with negative values of $M_{\ell e}$ and N_{des}, indicating remelting and grain destruction, is shown. (For interpretation of the references to colour in this Figure legend, the reader is referred to the web version of this article)

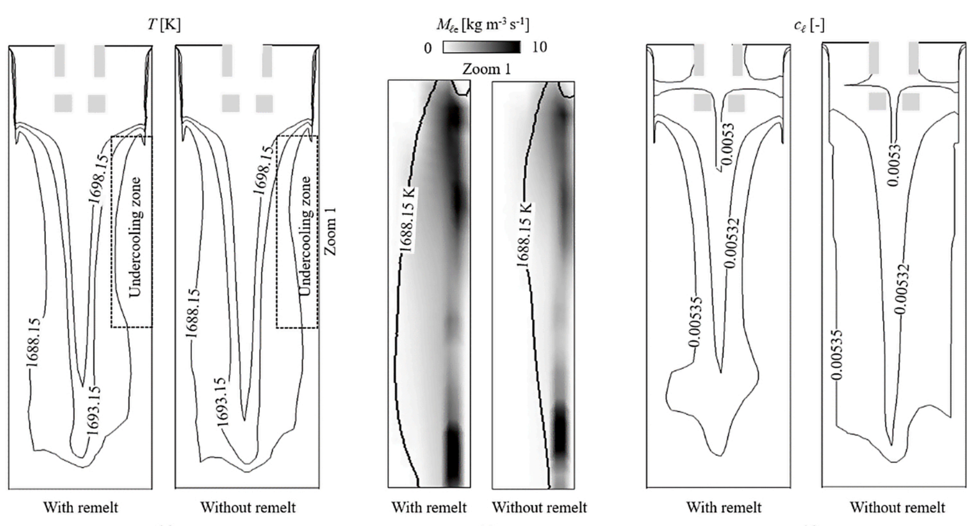

Fig. 11. Effect of remelting on the temperature (T) and liquid concentration (c_ℓ) fields, and a comparison of two simulation cases: one considering remelting, and one ignoring remelting. (a) T field and net mass transfer rate ($M_{\ell e}$). (b) Liquid concentration (c_ℓ).

Lorentz force (F_L) in the strand. No significant differences were found between the two cases. The Lorentz force in the melt front of the solidified shell in the second case was only 3% lower than that in the first case. Such a small difference in F_L did not significantly impact the initial solidification of the strand.

4.3. Shielding effect of the copper mold

The shielding effect of the copper mold on the rotational magnetic field depends on the operating temperature of the mold because its electrical conductivity (σ_m) is a function of temperature. To understand the influence of the shielding effect on the operating efficiency of M-EMS, two simulation cases were compared. The first case assumed a mold operating temperature of 298 K (corresponding to $\sigma_{m\text{-}298} = 4.7 \times 10^7$ S/m); the second case used a mold operating temperature of 423 K (corresponding to $\sigma_{m\text{-}423} = 3.18 \times 10^7$ S/m). Fig. 13(a) displays the time-averaged results of the magnetic flux density (B) and induced current density (J) on the mold surface for the two mold temperatures. B was minimally affected by the mold operating temperature, but J displayed a large difference between the two cases. The difference in the peak value of J at the edge of the mold reached approximately 35 %. The induced J created a secondary magnetic field directed opposite to the applied magnetic field. Thus, a so-called "shielding effect" was induced, and the applied magnetic field was weakened in the strand. Fig. 13(b) shows the contour of the Lorentz force (F_L) on the central longitudinal plane of the strand. Because of the stronger mold shielding effect at 298 K than that at 423 K, the F_L of the strand was visibly lower, resulting in an approximately 23.6 % reduction in F_L at the solidification front. This subsequently influenced the initial solidification in the mold region. For the shielding effect at room temperature (298 K), the average solid fraction in the strand of the mold region was reduced by 0.37 % compared to that at 423 K. In other words, to model the solidification of continuous casting under M-EMS properly, the shielding effect of the copper mold at an elevated operating temperature should be considered.

4.4. Electrical current path through the strand mold interface

During the continuous casting of steel, there is a slag layer between the strand and the copper mold. It is known that the electrical conductivity of the slag affects the electric current path, thereby influencing the M-EMS efficiency. Here, two extreme simulation cases are compared: conducting wall (i.e., the strand–mold interface is an ideal electrical conductor) and isolating wall (i.e., the strand–mold interface is an ideal electrical insulator). The modeling results for the two cases are shown in Fig. 14. The B fields were almost identical, but the J fields were extremely different between the two cases. The electrical conductivity of the mold (3.18×10^7 S/m) was considerably higher (38.78×) than that of the strand (8.2×10^5 S/m). The path of the induced electric current depends strongly on the strand–mold interface condition. As shown in Fig. 14(b), the induced current inside the strand was confined in the strand when the isolating wall condition was applied, while when the conducting wall condition was applied, the induced electric current was largely confined near the mold. For the latter case with a conducting wall, the maximum J occurred at the mold exit. When the isolating wall was applied, F_L showed a symmetric distribution and reached the maximum value at the strand surface in the middle section of the stirrer. However, for the conducting wall condition, three F_L peaks were observed: one at the strand surface in the middle section of the stirrer and two on the strand surface near the mold exit. Overall, the F_L generated in the strand was relatively low when the conducting wall condition was applied. In the isolating wall case, the average solid fraction in the strand of the mold region was predicted to be approximately 0.61 % more than that of the conducting wall case. The actual electrical conductivity of the strand–mold gap is unknown. Considering that (1) the slag layer in the strand–mold gap is mostly in the solid state, which has a relatively lower conductivity, and (2) an air gap may occasionally form between the strand and mold, the strand–mold interface should be treated as an electrically isolating wall.

4.5. Model uncertainty analysis

Although the three-phase solidification model has been consistently evaluated against different industry castings and laboratory experiments by Wu et al. (2019), this study is the first of its kind to apply it to solidification in billet continuous casting with M-EMS. The agreement between the as-cast structure of the simulation and that of the experiment (Fig. 8(a)-(b)) may only be considered as demonstrative, because the modeling results are largely dependent on the modeling parameters, which are partially unknown. Among others, such as the temperature-dependent thermophysical properties and thermal boundary conditions, the main uncertain parameters are the heterogeneous nucleation parameters (n_{in}^0, ΔT_N, and ΔT_σ) and the coefficient that governs crystal fragmentation (γ). The criterion for the estimation of the nucleation parameters is based on the industry practice whereby a dominant columnar structure should appear in the billet in the as-cast strand for the case without M-EMS; hence, the number of potential nucleation sites should be relatively small ($n_{in}^0 = 10^9$ m^{-3}). Both, industry practice and the current simulations (Table 3) agree that the main origin of equiaxed crystals with M-EMS is crystal fragmentation; therefore, the determination of γ becomes more crucial. The topic of M-EMS-induced crystal fragmentation, as the origin of equiaxed crystals in continuously cast steel, is actually under-researched. Here,γ (3.0×10^{-5}) was obtained through a parameter study by matching the as-cast structure of the simulation with the experimental one shown in Fig. 8(a).

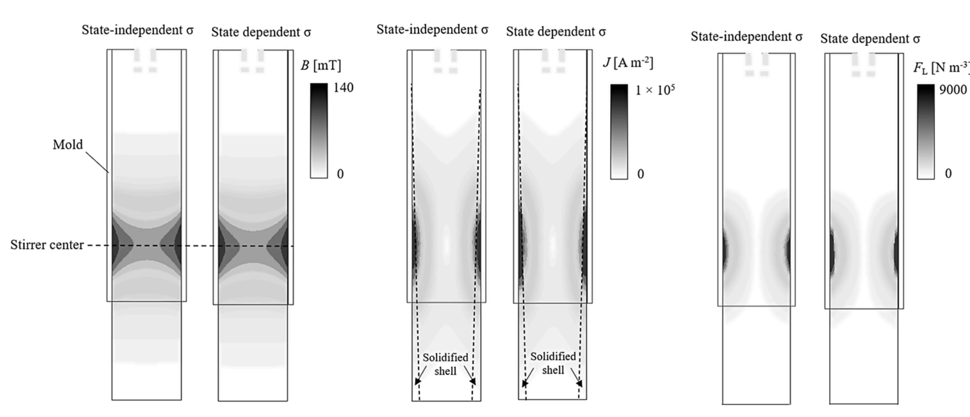

Fig. 12. Time-averaged magnitude of (a) magnetic flux density (B), (b) induced electrical current density (J), and (c) Lorentz force (F_L). Two simulation cases are compared, that consider and ignore the state-dependent electrical conductivity (σ).

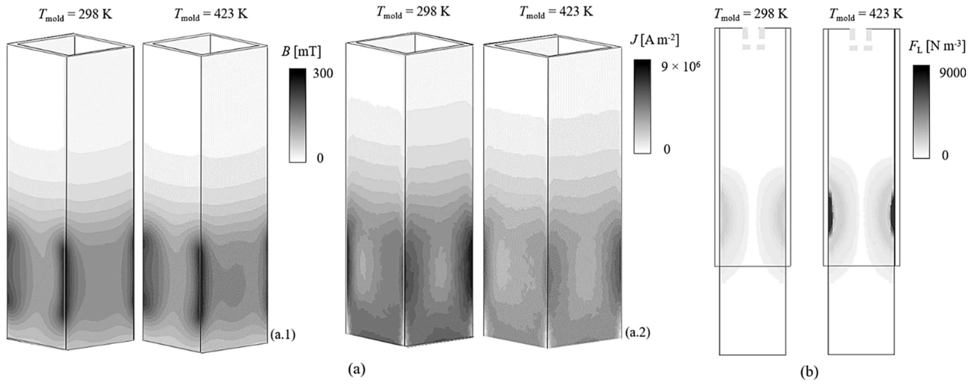

Fig. 13. (a) Time-averaged magnitude of electromagnetic fields on the mold surface at two different mold temperatures: (a.1) magnetic flux density (B) and (a.2) induced current density (J). (b) Contour of the Lorentz force (F_L) on the central longitudinal plane of the strand.

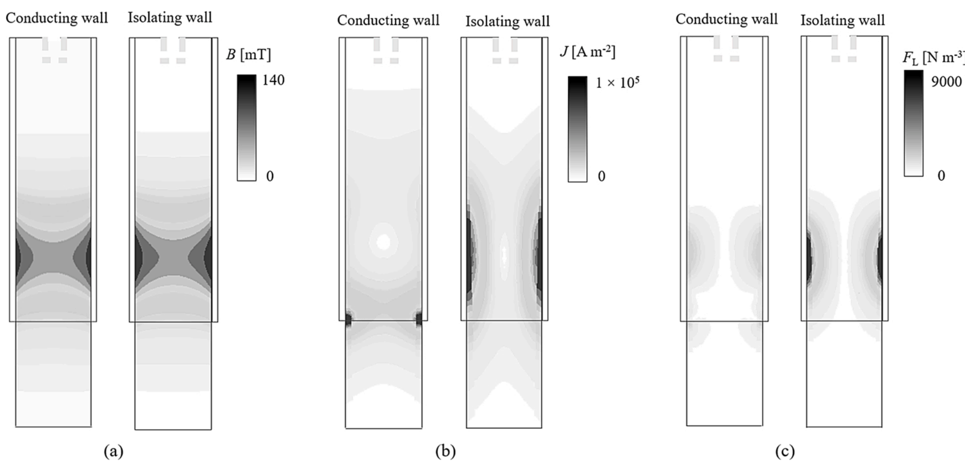

Fig. 14. Time-averaged magnitude of the (a) magnetic flux density (B), (b) induced electrical current density (J), and (c) Lorentz force (F_L). Two simulation cases are compared: conducting wall (i.e., the strand–mold interface is an ideal electrical conductor) and isolating wall (i.e., the strand–mold interface is an ideal electrical insulator).

Note that for both simulation cases (with and without M-EMS), the same set of nucleation and fragmentation parameters was used.

Another important parameter that significantly impacts macrosegregation, as induced by equiaxed crystal sedimentation, is the volume ratio of the solid dendrite to the equiaxed grain envelope (f_{si}). Because more porous dendritic crystals (smaller f_{si}) tend to pack earlier, that is, at a lower volume fraction of solid (f_e), the induced negative macrosegregation (c_{mix}^{index}) in the central equiaxed zone is less intensive. A recent numerical parameter study showed that the intensity of the negative segregation in the equiaxed sedimentation zone is linearly proportional to f_{si}. Furthermore, f_{si} is alloy-dependent. Owing to the lack of experimental data (macrosegregation map) for the alloy in this casting format, a value of 0.3 for f_{si} was arbitrarily chosen in this study. This implies that the calculated macrosegregation intensity (Fig. 9), particularly in the central equiaxed zone, was quantitatively inaccurate. However, the calculated segregation pattern is qualitatively reliable because the model considers key mechanisms of macrosegregation in the casting process.

5. Conclusion

A three-phase solidification model was used to investigate mixed columnar–equiaxed solidification in the continuous casting of a steel billet under the effect of M-EMS. The major contribution of this work is to demonstrate the role of M-EMS in the control of mold flow, which further impacts superheat dissipation, crystal fragmentation, and the subsequent formation of the as-cast structure and macrosegregation. The following conclusions were drawn.

(1) In billet casting using existing casting geometry (195 × 195 mm), M-EMS played the following two roles: i) to accelerate superheat dissipation in the mold region, leaving the liquid core out of the mold region largely undercooled, and ii) to promote the formation of equiaxed crystals through M-EMS-induced crystal fragmentation. These roles were fulfilled synergistically, to result in a central equiaxed zone: the latter led to the origin and formation of equiaxed crystals, and the former promoted the survival and further growth of equiaxed crystals in the secondary cooling zone. By explicitly noting the casting format, we stress that the above roles will change with the casting size and geometry.

(2) The central equiaxed structure observed in the practice of billet casting with M-EMS was attributed to crystal fragmentation rather than heterogeneous nucleation. The numerical model verified that the crystal fragmentation rate is very sensitive to the M-EMS implementation, whereas the heterogeneous nucleation rate was not.

(3) A small portion of equiaxed crystals could be brought by the M-EMS-induced swirling flow into the superheated zone and remelted. These simultaneous phenomena (solidification at one location and grain migration and remelting at another location) represent an important species/energy transport mechanism, which impacts the as-cast structure and compositional heterogeneity.

(4) Numerical parameter studies were performed to investigate the shielding effect of the copper mold at different operating temperatures, including the effect of the (solid/liquid) state-dependent electrical conductivity of the strand and the effect of the electric current path through the strand–mold interface. Only the electric current path through the strand–mold interface was found to be of critical importance, and it significantly affected the M-EMS efficiency.

Although a satisfactory agreement between the numerically calculated and experimentally determined as-cast structure was achieved, the current modeling results can only be considered qualitative because some modeling parameters were estimated based on a numerical parameter study. Further laboratory or in-plant experiments are required to quantify these parameters.

Author declaration

The authors declare that they have no known competing financial interests or personal relationships that could have appeared to influence the work reported in this paper.

CRediT authorship contribution statement

Zhao Zhang: Conceptualization, Methodology, Software, Investigation, Writing - original draft, Visualization. **Menghuai Wu:** Conceptualization, Methodology, Software, Writing - review & editing, Project administration, Funding acquisition. **Haijie Zhang:** Methodology, Software. **Susanne Hahn:** Validation, Funding acquisition. **Franz Wimmer:** Investigation. **Andreas Ludwig:** Resources, Supervision. **Abdellah Kharicha:** Software, Formal analysis.

Declaration of Competing Interest

None.

Acknowledgements

The authors acknowledge the financial support from the Austria Research Promotion Agency (FFG) through the Bridge 1 project (No. 868070) as well as the technical support of the industrial partner Primetals Technologies Austria GmbH.

References

An, H., Bao, Y., Wang, M., Zhao, L., 2018. Effects of electromagnetic stirring on fluid flow and temperature distribution in billet continuous casting mould and solidification structure of 55SiCr. Metall. Res. Technol. 115, 103–115. https://doi.org/10.1051/metal/2017075.

An, H., Bao, Y., Wang, M., Yang, Q., Huang, Y., 2019. Improvement of centre segregation in continuous casting bloom and the resulting carbide homogeneity in bearing steel GCr15. Ironmak. Steelmak. 46, 896–905. https://doi.org/10.1080/03019233.2019.1604614.

Ayata, K., Mori, T., Fujimoto, T., Ohnishi, T., Wakasugi, I., 1984. Improvement of macrosegregation in continuously cast bloom and billet by electromagnetic stirring. Trans. Iron Steel Inst. Japan 24, 931–939. https://doi.org/10.2355/isijinternational1966.24.931.

Du, W.D., Wang, K., Song, C.J., Li, H.G., Jiang, M.W., Zhai, Q.J., Zhao, P., 2008. Effect of special combined electromagnetic stirring mode on macrosegregation of high strength spring steel blooms. Ironmak. Steelmak. 35, 153–156. https://doi.org/10.1179/030192307X239533.

Du, F., Zhang, K., Li, C., Chen, W., Zhang, P., Wang, X., 2021. Investigation on non-uniform friction behaviors of slab during continuous casting based on an inverse algorithm. J. Mater. Process. Technol. 288, 116871 https://doi.org/10.1016/j.jmatprotec.2020.116871.

Fang, Q., Ni, H., Wang, B., Zhang, H., Ye, F., 2017. Effects of EMS induced flow on solidification and solute transport in bloom mold. Metals (Basel). 7, 72. https://doi.org/10.3390/met7030072.

Han, Q., Hellawell, A., 1997. Primary particle melting rates and equiaxed grain nucleation. Metall. Mater. Trans. B Process Metall. Mater. Process. Sci. 28, 169–173. https://doi.org/10.1007/s11663-997-0139-7.

Janik, M., Dyja, H., 2004. Modelling of three-dimensional temperature field inside the mould during continuous casting of steel. J. Mater. Process. Technol. 157–158, 177–182. https://doi.org/10.1016/j.jmatprotec.2004.09.026.

Jia, Y., Hou, J., Wang, H., Le, Q., Lan, Q., Chen, X., Bao, L., 2020. Effects of an oscillation electromagnetic field on grain refinement and Al8Mn5 phase formation during direct-chill casting of AZ31B magnesium alloy. J. Mater. Process. Technol. 278, 116542 https://doi.org/10.1016/j.jmatprotec.2019.116542.

Kunstreich, S., 2003a. Electromagnetic stirring for continuous casting - Part 1. Rev. Metall. Cah. D'Informations Tech. 100, 395–408. https://doi.org/10.1051/metal:2003198.

Kunstreich, S., 2003b. Electromagnetic stirring for continuous casting - Part 2. Rev. Metall. Cah. D'Informations Tech. 100, 1043–1061. https://doi.org/10.1051/metal:2003113.

Laitinen, E., Neittaanmäki, P., 1988. On numerical simulation of the continuous casting process. J. Eng. Math. 22, 335–354. https://doi.org/10.1007/BF00058513.

Li, J., Wang, B., Ma, Y., Cui, J., 2006. Effect of complex electromagnetic stirring on inner quality of high carbon steel bloom. Mater. Sci. Eng. A 425, 201–204. https://doi.org/10.1016/j.msea.2006.03.061.

Li, S., Lan, P., Tang, H., Tie, Z., Zhang, J., 2018. Study on the electromagnetic field, fluid flow, and solidification in a bloom continuous casting mold by numerical simulation. Steel Res. Int. 89, 1800071 https://doi.org/10.1002/srin.201800071.

Li, S., Xiao, H., Wang, P., Liu, H., Zhang, J., 2019. Analysis on electromagnetic field of continuous casting mold including a new integral method for calculating electromagnetic torque. Metals (Basel). 9, 946. https://doi.org/10.3390/met9090946.

Li, H., Gong, M., Li, T., Wang, Z., Wang, G., 2020. Effects of hot-core heavy reduction rolling during continuous casting on microstructures and mechanical properties of hot-rolled plates. J. Mater. Process. Technol. 283, 116708 https://doi.org/10.1016/j.jmatprotec.2020.116708.

Lipton, J., Glicksman, M.E., Kurz, W., 1984. Dendritic growth into undercooled alloy metals. Mater. Sci. Eng. 65, 57–63. https://doi.org/10.1016/0025-5416(84)90199-X.

Natarajan, T.T., El-Kaddah, N., 2004. Finite element analysis of electromagnetic and fluid flow phenomena in rotary electromagnetic stirring of steel. Appl. Math. Model. 28, 47–61. https://doi.org/10.1016/S0307-904X(03)00114-8.

Peel, D.A., Pengelly, A.E., 1968. Heat transfer, solidification, and metallurgical structure in the continuous casting of aluminum. Proc. of 1st SP Conf. in 1967. The Solidification of Metals 186–196.

Spitzer, K.H., Dubke, M., Schwerdtfeger, K., 1986. Rotational electromagnetic stirring in continuous casting of round strands. Metall. Trans. B 17, 119–131. https://doi.org/10.1007/BF02670825.

Sun, H., Zhang, J., 2014. Study on the macrosegregation behavior for the bloom continuous casting: Model development and validation. Metall. Mater. Trans. B. 45, 1133–1149. https://doi.org/10.1007/s11663-013-9986-6.

Thomas, B.G., 2018. Review on modeling and simulation of continuous casting. Steel Res. Int. 89, 1700312 https://doi.org/10.1002/srin.201700312.

Thomas, B.G., Singh, R., Vanka, S.P., Timmel, K., Eckert, S., Gerbeth, G., 2015. Effect of single-ruler electromagnetic braking (EMBr) location on transient flow in continuous casting. J. Manuf. Sci. Prod. 15, 93–104. https://doi.org/10.1515/jmsp-2014-0047.

Trindade, L.B., Vilela, A.C.F., Filho, A.F.F., Vilhena, M.T.M.B., Soares, R.B., 2002. Numerical model of electromagnetic stirring for continuous casting billets. IEEE Trans. Magn. 38, 3658–3660. https://doi.org/10.1109/TMAG.2002.804804.

Trindade, L.B., Nadalon, J.E.A., Contini, A.C., Barroso, R.C., 2017. Modeling of solidification in continuous casting round billet with mold electromagnetic stirring (M-EMS). Steel Res. Int. 88, 1600319. https://doi.org/10.1002/srin.201600319.

Wang, X., Tang, L., Zang, X., Yao, M., 2012. Mold transient heat transfer behavior based on measurement and inverse analysis of slab continuous casting. J. Mater. Process. Technol. 212, 1811–1818. https://doi.org/10.1016/j.jmatprotec.2012.04.001.

Wang, S., Alvarez De Toledo, G., Välimaa, K., Louhenkilpi, S., 2014. Magnetohydrodynamic phenomena, fluid control and computational modeling in the continuous casting of billet and bloom. ISIJ Int. 54, 2273–2282. https://doi.org/10.2355/isijinternational.54.2273.

Wang, X., Zheng, S., Liu, Z., Zhu, M., 2020a. Numerical simulation on multiple physical fields behaviors in billet continuous casting with different stirrer positions. Steel Res. Int. 91, 1900415 https://doi.org/10.1002/srin.201900415.

Wang, Y., Chen, W., Jiang, D., Zhang, L., 2020b. Effect of the gap between copper mold and solidified shell on the fluid flow in the continuous casting strand with mold electromagnetic stirring. Steel Res. Int. 91, 1900470 https://doi.org/10.1002/srin.201900470.

Wang, Y., Zhang, L., Yang, W., Ji, S., Ren, Y., 2021. Effect of mold electromagnetic stirring and final electromagnetic stirring on the solidification structure and macrosegregation in bloom continuous casting. Steel Res. Int. 92, 2000661 https://doi.org/10.1002/srin.202000661.

Wu, M., Ludwig, A., 2006. A three-phase model for mixed columnar-equiaxed solidification. Metall. Mater. Trans. A. 37, 1613–1631. https://doi.org/10.1007/s11661-006-0104-0.

Wu, H.J., Wei, N., Bao, Y.P., Wang, G.X., Xiao, C.P., Liu, J.J., 2011. Effect of M-EMS on the solidification structure of a steel billet. Int. J. Miner. Metall. Mater. 18, 159–164. https://doi.org/10.1007/s12613-011-0416-y.

Wu, M., Ludwig, A., Kharicha, A., 2019. Volume-averaged modeling of multiphase flow phenomena during alloy solidification. Metals (Basel) 9, 229. https://doi.org/10.3390/met9020229.

Zappulla, M.L.S., Cho, S.M., Koric, S., Lee, H.J., Kim, S.H., Thomas, B.G., 2020. Multiphysics modeling of continuous casting of stainless steel. J. Mater. Process. Technol. 278, 116469 https://doi.org/10.1016/j.jmatprotec.2019.116469.

Zhang, W., Luo, S., Chen, Y., Wang, W., Zhu, M., 2019. Numerical simulation of fluid flow, heat transfer, species transfer, and solidification in billet continuous casting mold with M-EMS. Metals (Basel) 9, 66. https://doi.org/10.3390/met9010066.
Zhang, H., Wu, M., Schumacher, P., Rodrigues, C.M.G., Ludwig, A., Kharicha, A., 2021. Modelling melting and grain destruction phenomena during globular equiaxed solidification. Appl. Math. Model. 97, 821–838. https://doi.org/10.1016/j.apm.2021.04.024.
Zheng, Y., Wu, M., Kharicha, A., Ludwig, A., 2018. Incorporation of fragmentation into a volume average solidification model. Model. Simul. Mater. Sci. Eng. 26, 015004 https://doi.org/10.1088/1361-651X/aa86c5.